RSC
Applied Interfaces

Accepted Manuscript

This article can be cited before page numbers have been issued, to do this please use: N. Das, A. Priyadarshini, S. Soren, M. K. Rana, D. Singha, B. C. Dhal, S. Swain, J. Panda, D. Soren and R. Sahu, *RSC Appl. Interfaces*, 2026, DOI: 10.1039/D6LF00091F.

ROYAL SOCIETY
OF CHEMISTRY

rsc.li/RSCApplInter

View Article Online
DOI: 10.1039/D6LF00091F

ARTICLE

Received 00th January 20xx,
Accepted 00th January 20xx

DOI: 10.1039/x0xx00000x

Pd@Ce Metal organic framework For Dual Reduction of Nitrophenols and Chromium (VI)

Niharika Das[a], Anulipsa Priyadarshini[a], Saraswati Soren[a], Malay Kumar Rana[c], Dipankar Singha[c], Bikash Chandra Dhal[a], Subrat Swain[a], Jagannath Panda[a,d], Daray Soren[a], Rojalin Sahu*[a,b]

*corresponding author: rsahufch@kiit.ac.in

Promising photocatalytic activities of Ce based materials, here in, a Cerium terephthalate metal organic framework (Ce-BDC) has been decorated with PdNPsvia double solvent method and established the characteristic features through PXRD, FTIR, FESEM, & BET surface area analysis. The excellent redox activity, electron transfer and unique photo-harvesting ability of the material demanded itself as an active member in the arena of photocatalyst materials. Interestingly these features were conveyed through the application in the degradation of environmental pollutants; as a representatives potassium dichromate ion (Cr(VI)) & 4-nitrophenol (4-NP) molecule. In particular, Its photo-responsive catalytic activity was evaluated in aqueous medium under room temperature for [Cr(VI)] and (4-NP) removal. Pd@Ce-BDC achieved ~94% reduction of 4-NP to 4-aminophenol within 10 min at room temperature ($k = 0.13\ \mathrm{min}^{-1}$), while ~95% of Cr(VI) was reduced to Cr(III) within 20 min under sunlight irradiation ($k = 0.206\ \mathrm{min}^{-1}$). These findings underscore the promise as highly efficient photocatalysts for environmental remediation, where the interplay of framework design and redox-active centers governs performance.

Introduction

Water, the foundation of life on Earth, is essential for all living beings. However, rapid population growth and industrialization have led to increasing problems of water scarcity and contamination worldwide.Noxious contaminants like heavy metals and industrial chemicals are becoming an increasing concern due to their persistence and toxicity. Among heavy metals, chromium is recognized as the second most hazardous pollutant after lead and is commonly found in wastewater discharged from textile, electroplating, and leather industries. Chromium exists mainly in two oxidation states: hexavalent chromium (Cr(VI)) and trivalent chromium (Cr(III)). Cr(VI) is highly toxic, a Group A carcinogen, water-soluble, and a proven mutagen, posing serious threats to both environmental and human health. Therefore, the reduction of Cr(VI) to the less toxic Cr(III) form is of great importance. Unlike Cr(VI), Cr(III) is an essential trace element for biological systems and tends to form insoluble hydroxides under controlled pH conditions, making it easier to remove from aqueous systems and safer for environmental applications.[1] Similarly, 4-NP is considered as a highly toxic pollutant found in pharmaceutical industries due to high stability and solubility in aqueous media. The presence of the nitro group ($-NO_2$) notably alters the electron density of the aromatic ring through strong inductive (-I) and resonance (-M) effects. As a result, the ring becomes more reactive and unstable, leading to the formation of harmful intermediates such as nitro radicals and nitroso compounds, which can disrupt biological functions by inducing methemoglobinemia through the oxidation of ferrous iron to ferric iron in haemoglobin[2, 3].

These two pollutants exhibit high biological and chemical stability in the environment. Consequently, the degradation of these pollutants using functional materials remains a key focus in environmental research[4]. Traditionally, Pd based complexes have been widely employed for catalytic applications due to their superior activity and selectivity compared to other noble NPs.They also exhibit strong interactions with hydrogen molecules, resulting efficient hydrogen activation for reduction of organic pollutants like nitroaromatic compounds[5].

---

[a] Future Materials Laboratory, School of Applied Sciences, Kalinga Institute of Industrial Technology (deemed to be university), Bhubaneswar, 751024
[b] Centre for Innovation and Research - Center for Next Generation Material and Technology (COIR-CNGMT), KIIT Deemed to be University, Bhubaneswar 751024, India
[c] Department of Chemistry, NIST University, Institute Park, Berhampur, Odisha, India
[d] IISER Berhampur, Berhampur Odisha 760010

Corresponding author: rsahufch@kiit.ac.in

View Article Online
DOI: 10.1039/D6LF00091F

Moreover, a well-known plasma effect of Pd NPs enables effective light harvesting, thereby promoting photocatalytic degradation of pollutants like Cr(VI)[6]. Despite these advantages, the practical application of Pd based catalysts are constrained byseparation and recovery, leading to poor recyclability and increased consumption of expensive metal like Pd[7, 8]. In addition single Pd NPs are easily aggregated during catalysis, resulting deactivation and rapid loss of activity of Pd NPs.To overcome these drawbacks, significant efforts have been directed towards engineering suitable catalyst supports to enhance Pd dispersion and reduce metal loading. A variety of support materials, including zeolites, silica, metal oxides, carbonaceous materials and organic polymers have been explored to improve catalytic efficiency and reusability, but these systems remains suboptimal due to NP agglomeration and metal leaching during catalytic cycles, which leads to activity loss[9]. In this context MOFs have emerged as highly promising supports for noble metal catalyst owing to their exceptionally (i) high surface area, adjustable pore structures and robust thermal stability. (ii) the unique functional groups on the organic linkerwithin MOFs can easily immobilise catalytically active metal ions, and avoids the loss of expensive metals and increase the stability[10-12].TheMetal-organic frameworks (MOFs), particularly lanthanides based MOFs, have attracted significant attention for catalysis.[13]Among them, cerium-based MOF (Ce-BDC) stands out due to the presence of Ce^{4+} ions with low-lying empty 4f orbitals, which contribute to their enhanced photocatalytic performance. These orbitals allow efficient LMCT, resulting in effective charge separation and reduced electron hole recombination rate as compared to other metal centers like Zr, Hf, Th, Ti, or U.[14] In addition, the redox metal centre Ce^{4+}/Ce^{3+} within Ce-BDC facilitates rapid electron transfer during redox processes, further enhancing its photocatalytic efficiency. Also their tunable structure, water stability, high porosity, and large surface area, which can be engineered to optimize adsorptive and catalytic properties for efficient pollutant removal[15].In this context, the interface formed between Pd NPs and Ce-BDC can modulate the electronic structure and promote efficient charge transfer, thereby significantly improving catalytic activity, stability and recyclability.Furthermore, Pd@Ce-BDC typically possess smaller band gaps (2.1 eV), enabling effective absorption of visible light and thus, significantly improving photocatalytic efficiency on light irradiation. Zhao et al. CeO_2@NiMOF has been used for the reduction of 4-NP to 4-AP; CeO_2 is chosen for its ability to provide abundant active sites, facilitate electron transfer, and synergize with Ni-MOF's adsorption capabilities, resulting in a highly efficient, selective, and stable catalyst.[16] Similarly, Kohantorabi et al. choose CeO_2 nanorods as the support for CuNi nanoparticles in their study on the catalytic reduction of 4-NP due to CeO_2 nanorods possess a superior surface oxygen release and storage capability, which is crucial for redox reactions involved in catalytic processes.[17] In another study, Anandkumar et al. highlights that the interaction at the interface between gold and cerium oxide, mainly redox cycling between Ce^{3+} and Ce^{4+}, are directly involved in the efficient hydrogenation of 4-NP to 4-AP[18].while Ce-MOFs like Ce-MOF-808 with Pd/Au support efficient for 4-NP reduction via enhanced electron transfer. Collectively, these studies highlight the versatility of Ce in improving catalytic performance by facilitating electron transfer and offering structural adaptability[19]. Also emphasize the critical role of surface area and redox-active centers in the rational design of efficient catalytic systems, as illustrated by selected examples in Table S1.

Building on these insights we have synthesized Pd@Ce-BDC) via a double solvent method, enabling immobilization of Pd NPs on Ce-BDC framework. The mixed valence Ce^{3+}/Ce^{4+} electronic structure of Ce-BDC, provides strong anchoring sites for Pd through electron donation, thereby lowering Pd adsorption energy and stabilizing Pd clusters against agglomeration[20]. The resulting Pd and Ce-BDC interface promotes efficient electron transfer, band gap narrowing, and accessible active sites. These synergistic effects collectively enhance catalytic activity, structural stability and recyclability making Pd@Ce-BDC an effective catalyst for both4-NP and Cr(VI) reduction.The photo-catalytic reduction using Pd@Ce-BDC was evaluated by optimising the parameters such as catalytic dosage, pH of the solution, etc.40 ppm of toxic Cr(VI) was reduced to Cr(III) at neutral pH (pH=7) and 0.5 mM of 4-NP reduced to 4-AP (pH=7) using 5 mg of Pd@Ce-BDC catalyst at room temperature using visible light source. Notably the catalyst retained its framework integrity up to the 8th cycle in 4-NP reduction and 7th cycle in Cr(VI) reduction underscoring robust stability and reusability.In contrast, pristine Ce-BDC exhibited significantly lower activity, reducing only 40 ppm Cr(VI) and 0.5 mM 4-NP under acidic conditions, emphasizing the role of Pd in modulating the electronic structure and catalytic efficiency of the Ce-BDC framework. The ability of Pd@Ce-BDC to operate efficiently under neutral pH and room temperature represents a substantial advantage for practical wastewater remediation, minimizing secondary chemical inputs while maintaining high catalytic efficiency.

Experimental

Synthesis of the Pd@Ce-MOF

Ce-BDC has been performed employing the reported procedure[21]. The PdNPs loaded Ce-BDC was prepared by using a double solvent method. In a typical experiment, 200 mg of Ce-BDC was dispersed in 40 ml of acetonitrile under continuous stirring to ensure uniform suspension. Separately, palladium acetate solution (0.1M) prepared in methanol was dropwise added to the Ce-BDC and the mixture was continuously stirred for 4h to facilitate the adsorption of Pd^{2+} within the Ce-BDC framework. The resulting solid was then filtered, washed with DI water and dried at 80◦C. Subsequently after dehydration freshly prepared $NaBH_4$ (0.05mM) was added under stirring leading to the formation of gray suspension, indicating the in situ reduction of Pd^{2+} to PdNPs as shown in Figure.4.1. The final product was recovered by centrifugation and dried at 100◦C to obtain Pd NPs decorated on Ce-BDC (Pd@Ce-BDC), which was used for subsequent catalytic studies[22].

Catalytic test for reduction of Cr(VI):

To evaluate the photocatalytic performance of the synthesized catalysts, Cr(VI) was selected as a representative toxic heavy metal pollutant. A 40 ppm aqueous solution of potassium dichromate ($K_2Cr_2O_7$) was prepared according to standard method. Prior to the experiment, the catalysts were activated for 10 hours and ground into fine powders. For the photocatalytic test, 5 mg of catalyst was dispersed in 30 mL of Cr(VI) solution and kept in the dark for 15 minutes to establish adsorption desorption equilibrium, allowing adsorption of Cr(VI) on surface of catalyst before light exposure. Following dark reaction, the suspension was exposed to light, and the Cr(VI) concentration was tracked using a JASCO V-770 UV-Vis spectrophotometer within the wavelength range of 300-450 nm. The absorbance of Cr(VI) solution decreased over time and completely diminished within 20 minutes, indicating efficient reduction of Cr(VI) to Cr(III) in neutral pH as shown in Figure 3a. To further investigate the reaction mechanism, the formation of H_2O_2 as a byproduct of the photocatalytic Cr(VI) reduction was confirmed by titrating the post-reaction $K_2Cr_2O_7$ solution with a standardized $KMnO_4$ solution (>99%, Sigma-Aldrich, Germany). This additional analysis provided insight into the redox processes involved during the photocatalytic degradation of Cr(VI) under sunlight[23, 24].

Catalytic test for 4-NP reduction:

The reduction of 4-NP using $NaBH_4$ was selected as another model reaction to evaluate the catalytic performance of Pd@Ce-BDC, using the same spectrophotometer employed for Cr(VI) analysis. The activation of the catalyst was performed as in the Cr(VI) reduction procedure, was used for the reduction of 4-NP. In a standard quartz cuvette having path length 1 cm, 1 mL of an aqueous 4-NP solution (0.5 mM) was mixed with 0.6 mL of freshly prepared aqueous $NaBH_4$ solution (0.05 mM). After thorough mixing, 1.5 mL of dispersed catalyst solution was introduced and tested at varying concentrations of 3, 5, and 10 mg at neutral pH[12, 25].

Results and discussion

The Ce-BDC MOF was synthesized via a hydrothermal method, wherein the Ce metal nodes were coordinated with terephthalic acid (BDC) linkers to construct a crystalline porous framework. The synthesized powder material was characterized with significant techniques. PXRD, XPS, RAMAN, TGA, FTIR etc confirmed regarding the coordination of Ce & BDC linkage and generation of photo responsive 'Ce-O' cluster. In this regard, the reported crystallographic information file collaborated with the PXRD pattern of synthesized powder compound. Therefore, the phase purity of material has been extremely similar to well-known Uio-66 framework. The insight of structural architecture reveal that the central metal ion displays an eight coordinated geometry, wherein Ce atoms are coordinated with BDC by two distinct types of oxygen environments.

View Article Online
DOI: 10.1039/D6LF00091F

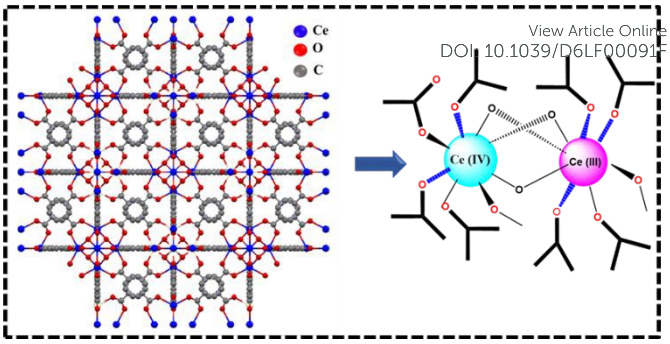

Figure 1: Schematic representation and molecular structures of the synthesized Ce-BDC

As depicted in Figure 1, the Ce(IV) ions display an eight-coordinated geometry, with each cerium atom participating in the hexanuclear cluster formed from six $Ce_6O_4(OH)_4$ secondary building units (SBUs). The triangular faces of each Ce(IV) cluster are alternately coordinated by μ_3-O and μ_3-OH groups, leading to the formation of a hexanuclear cluster denoted as $Ce_6(\mu_3\text{-}O)_4(\mu_3\text{-}OH)_4^{2+}$[26]. The BDC ligand contains two carboxylate groups ($-COO^-$), each with two oxygen atoms. These carboxylate groups act as bidentate ligands, enabling them to bind simultaneously to a single cerium ion through both oxygen atoms. This interaction creates a stable coordination environment around the cerium ion, enhancing the stability and functionality of the Ce-BDC complex[27]. This structure provides accessible cerium sites for reactions and exhibits reversible Ce^{4+}/Ce^{3+} redox transitions due to the stabilization of mixed oxidation states within the framework, attributed to delocalized π-electrons in terephthalate ligands that facilitate electron transfer[28].

The crystallinity and phase purity of Ce-BDC and Pd@Ce-BDC were analyzed using Powder X-ray Diffraction (PXRD) within the 2θ range of 5–50°. The PXRD pattern of Ce-BDC MOF exhibits sharp reflections at 2θ values of 7.2°, 8.3°, 11.7°, 13.8°, and 14.4°, corresponding to the (111), (200), (220), (311), and (222) planes, respectively. These peaks closely correspond to those reported in the literature, confirming the well-crystallized nature, high structural integrity, and successful synthesis of Ce-BDC as validated by PXRD analysis[28, 29]. The diffraction pattern of Pd@Ce-BDC closely matches with that of Ce-BDC, indicating that PdNP loading does not alter the crystalline phase or disrupt the framework integrity of the MOF support as shown in Figure 2a.

FTIR analysis confirmed the presence of functional groups in the organic linkers and revealed the coordination of metal ions, indicating successful framework formation as depicted in Figure.4.5. In Ce-BDC, a distinct peak at 511 cm^{-1} corresponds to Ce–O vibrations, while bands between 1000–1200 cm^{-1} and at 737 cm^{-1} are assigned to C–O stretching and O–H bending of the H_2BDC ligand. These collectively confirm the coordination of BDC to cerium centers and the presence of key structural units essential for the Ce-BDC framework as shown in Figure 2b[30, 31]. The absence of appearance of new peak after Pd NPs loading indicating stable coordination environment which is aritibuted to the low Pd loading and high dispersion within the framework.FESEM analysis of Ce-BDC revealed the presence of irregularly shaped, intergrown nanoparticles with a tendency to form aggregated clusters. The particles displayed rough

View Article Online
DOI: 10.1039/D6LF00091F

surfaces and heterogeneous morphology matches with literature. After the deposition the overall framework remain intact[32], indicating no significant structural damages, leading to the formation of PdNPs and Ce-BDC interface. Furthermore, energy dispersive X-ray (EDX) analysis confirms the presence of Pd, with loading approximately 2.0 wt%, indicating successful incorporation of Pd on Ce-BDC MOF (Figure S1-S4).Furthermore, nanoparticle deposition on Ce-BDC can be confirmed through MOF. Upon PdNP deposition the BET surface area decreased from 544 m^2/g to 61 m^2/g accompanied by a reduction in pore volume from0.24 to 0.08 cm^3/g. this confirms PdNP incorporation on porous support like Ce-BDC (Figure S5).

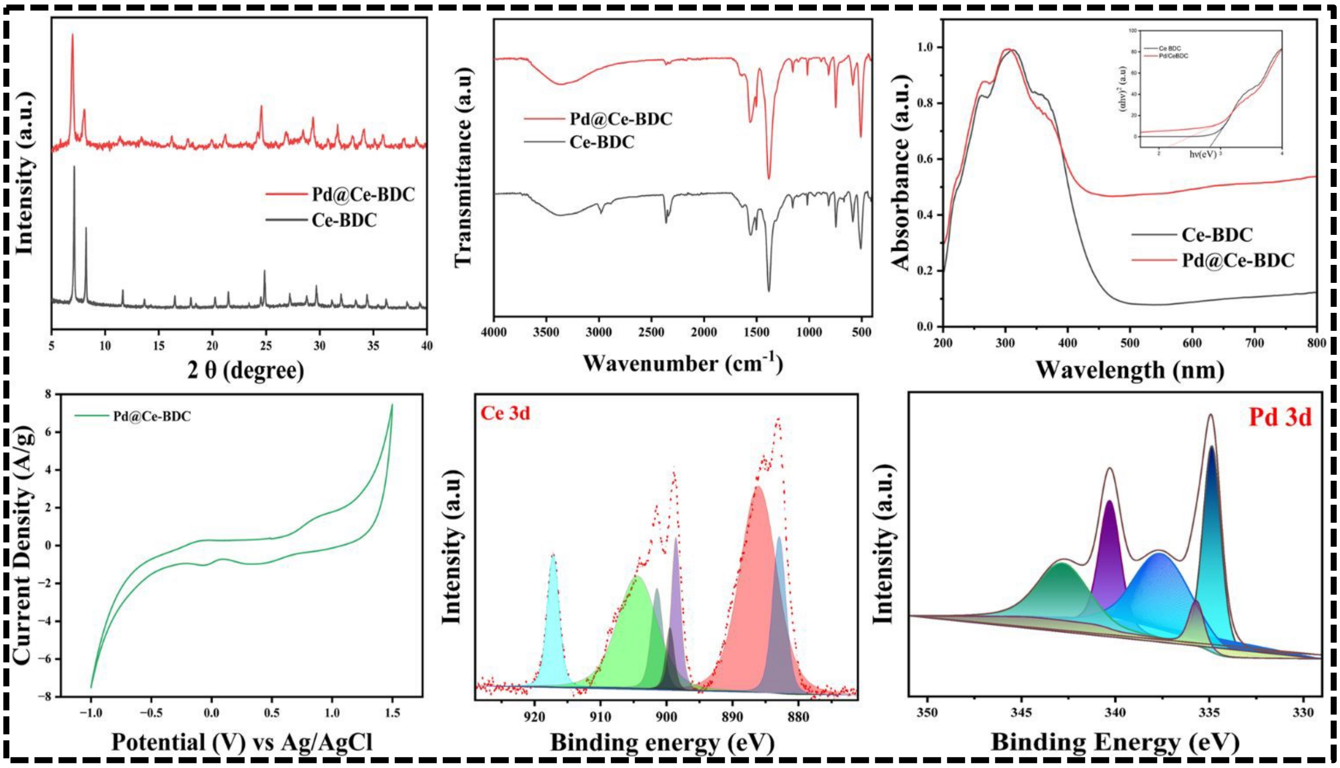

Figure 2: (a) PXRD, (**b)**FTIR **(c)**UV-DRS spectra of Ce-BDC**(d)**N_2 adsorption-desorption isotherms, **(e)**Cyclic voltammetry **(f)**XPS peaks of Ce 3d **(g)**Pd 3d of Pd@Ce-BDC

The semiconducting nature of Ce-BDC, a key factor for photocatalysis, was evaluated using UV-Vis DRS, which revealed distinct optical absorption characteristics.The UV–Vis diffuse reflectance spectrum of the Ce-BDC MOF exhibits strong absorption in the ultraviolet region (~200–350 nm)[33, 34], which originates from π–π* electronic transitions of the BDC organic linker along with ligand-to-metal charge transfer (LMCT) from carboxylate 2p orbitals to the Ce 4f/5d states[15, 35]. A gradual absorption tail extending into the visible region is also observed, which can be ascribed to the coexistence of Ce^{3+}/Ce^{4+} redox couples that promote enhanced light absorption. Upon loading of Pd nanoparticles, the absorption edge shows a slight blue shift, indicating electronic interaction between the Pd species and the Ce-BDC framework. Correspondingly, the optical band gap decreases from 2.7 eV for pristine Ce-BDC to 2.1 eV for Pd@Ce-BDC, demonstrating that Pd incorporation effectively narrows the band gap and improves facilitating electron transfer during reduction of 4-NP as depicted in Figure 2c. XPS analysis was performed to gain detailed insights into the elemental composition, chemical states, and surface interactions of the material. Furthermore to study the elemental composition and surface chemical state of Pd NP immobilised on Ce-BDC were analyzed by XPS as shown inFigure 2 d. The survey spectrum verifies the existence of Pd in addition to the framework constituents namely C, N, O and Ce. Indicating the successful incorporation of Pd on the Ce-BDC support. The high resolution C 1s spectrum can be deconvoluted in to multiple components with peak corresponding to sp^2 hybridized carbon at 284.5 eV and oxygen containing carbon species appearing at higher binding energies between 285 and 289 eV reflecting the functional group of Ce-BDC (Figure S7a& Figure S7 b). This Ce 3d indicates the coexistence of both Ce^{4+} and Ce^{3+} oxidation states. Specifically, Ce^{4+} characterized by peaks at $3d_{3/2}$ (918.4, 901.1, 899.1 eV) and $3d_{5/2}$ (882.4 eV). The peaks at 904.4 and 885.9 eV correspond to Ce^{3+} states in $3d_{3/2}$ and $3d_{5/2}$, respectively. These findings indicate that the Ce-BDC framework exhibits a mixed valence state involving both Ce^{3+} and Ce^{4+}, responsible for its redox activity[36-38]. The Pd 3d core level spectrum exhibits characteristic doublets corresponding to different Pd chemical state. The peaks appearing at approximately 336 and 341 eV are attributed to Pd $3d_{5/2}$ and Pd $3d_{3/2}$ levels of metallic Pd0, respectively. In contrast the signals observed at around 338 and 343 eV corresponds to the Pd $3d_{5/2}$ and Pd $3d_{3/2}$ components of Pd^{2+}species. The partial oxidation of Pd^{2+} is ascribed to strong interactions between Pd and surface

View Article Online
DOI: 10.1039/D5LF00391D

absorbed oxygen which improve the adherence of Pd on Ce-BDC support, provides stable anchoring sites and structural stability[9].The specific binding energies and the relative proportion of Ce^{3+} and Ce^{4+} responsible for redox properties in framework.

Cyclic voltammetry (CV) experiments were conducted to investigate the redox behavior of the prepared MOFs. It exhibitdistinct and reversible redox peaks, supporting fast electron transfer and reversible Ce^{3+}& Ce^{4+} cycling under applied potentials. The electrode performance was evaluated at various scan rates 100 mV/s using a three-electrode configuration in a mixed electrolyte solution of 3M Na_2SO_4. The resulting CV curves displayed well-defined redox peaks within the range of 1.0 to 1.5 V. Redox pair for Ce(IV)/Ce(III) around 0.3–0.5 V (anodic) and -0.1 to 0.0 V (cathodic) vs. Ag/AgCl, reflecting reversible mixed-valence cerium states enhanced by the MOF's porosity and ligand coordination. Pd incorporation shifts or amplifies these peaks (e.g., anodic ~0.4 V, cathodic ~-0.05 V), with additional Pd(0)/Pd(II) oxidation near 0.8–0.9 V, matching your observed 0.89 V peak[9, 38].

Photo catalytic reduction of Cr(VI) using Pd@Ce-BDC

The photocatalytic reduction of Cr(VI) using Pd@Ce-BDC as a catalyst was attributed to its enhanced electron transfer and visible light harvesting ability. The results demonstrated complete removal of 40 ppm Cr(VI) within 20 minutes using only 5 mg of the catalyst, highlighting its high efficiency as shown in Figure 3a. The degradation efficiency was calculated using the equation [22, 34]:

$$\%\, of Cr(VI) reduction = \left(1-\frac{Ct}{C0}\right)\times 100\% = \left(1-\frac{At}{A0}\right)\times 100 \quad \text{(eq.1)}$$

Where C_t and C_0 represents the concentration of Cr(VI) at different time t and initial concentration, whereas A_t and A_0 represents the absorbance at 370 nm at time t and at the initial moment. The kinetics of the photocatalytic reduction followed a pseudo first order kinetics, expressed by the equation (eq. 2)[39]:

$$ln(C_0/C_t) = kt \quad \text{(eq.2)}$$

where k, and t represent the observed rate constant, and reaction time, respectively as shown in Fig 5a, the plot of ln (C_0/C_t) vs time results a straight line from which the rate constant (k) was determined to be 0.11 min^{-1} with correlation coefficients (R^2) >0.99 as shown in Figure 3b.

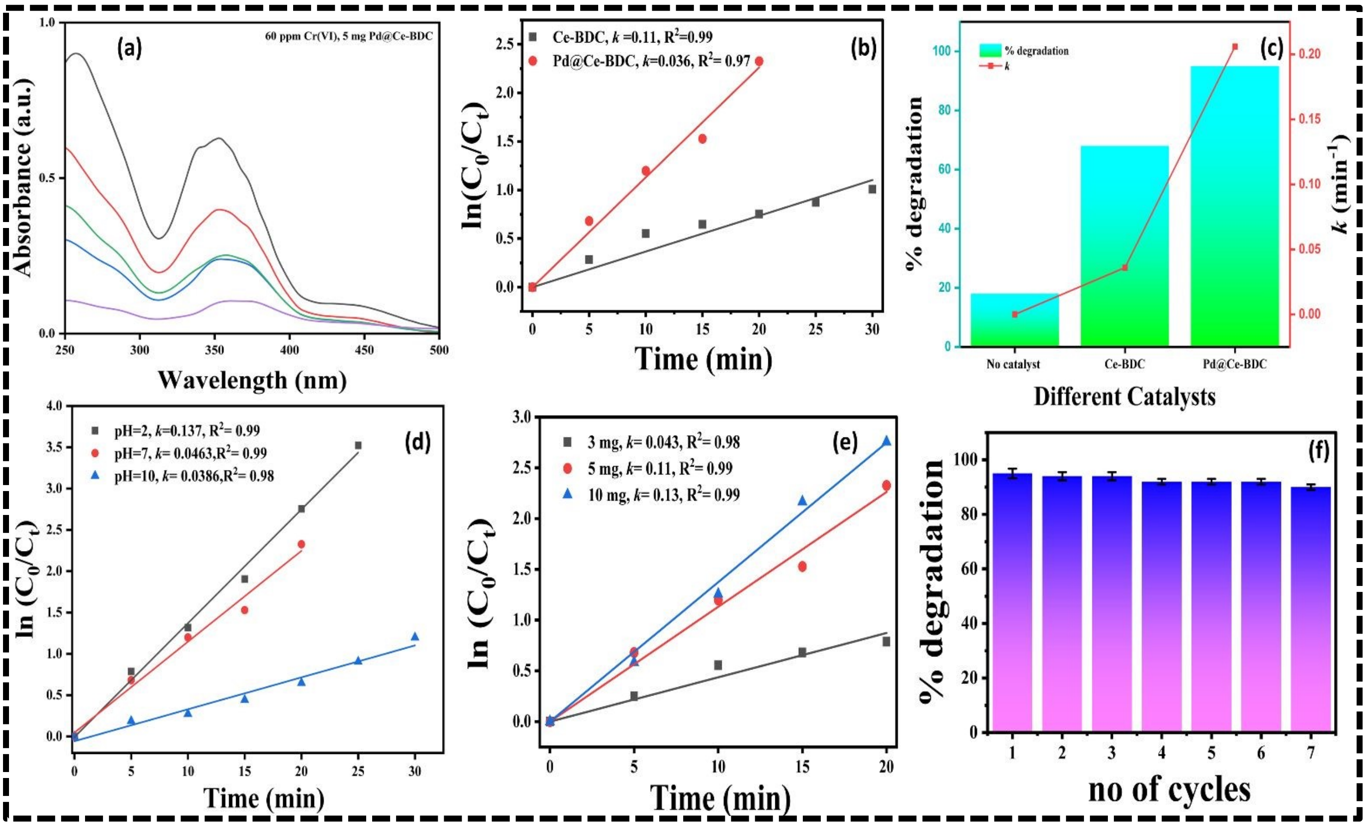

Figure 3: (a) Uv-Vis spectra,**(b)** Pseudo-first-order kinetic models of Cr(VI) reduction using Ce-BDC & Pd@Ce-BDC**(c)** histogram of k value with % efficiency vs catalytic dosage for Cr(VI) reduction**(d)** $ln(C_t/C_0)$ vs time for different pH,**(e)**$ln(C_t/C_0)$ vs time for different dosage (f) histogram showing reusability after Cr(VI) reduction

The catalyst dosages were optimized as 5 mg by maintaining a constant concentration of 40 ppm Cr (VI) solution. By increasing the catalyst dosage from 3 mg to 10 mg, both the rate of reaction and catalytic efficiency improved significantly.

View Article Online
DOI: 10.1039/D6LF00091E

The rate constant for 3 mg of Pd@Ce-BDC catalyst was found to be 0.043 min^{-1} with a reduction efficiency of 68.3%.Upon increasing the dosage to 10 mg, the rate of reaction and efficiency drastically increased to 0.13 min^{-1} and 93.9% respectively as plotted in Figure 3e. This improvement is attributed to the greater number of available active sites, enabling enhanced interaction between the catalyst and Cr(VI) species. However, the slight increase in rate constant and efficiency when increasing the dosage from 5 mg to 10 mg is likely due to the saturation of active sites and possible mass transfer limitations, resulting in only marginal performance gains. The reduction rate of hexavalent chromium is strongly influenced by pH. The pseudo-first-order rate constant decreased from 0.13 min^{-1} to 0.038 min^{-1} by increasing the pH from 2 to 10, as shown in Figure 3d. This may be due to the fact that, at acidic and neutral pH, Cr(VI) ($HCrO_4^-$ or $Cr_2O_7^{2-}$) carry a negative charge, while the Pd@Ce-BDC surface may become positively charged due to protonation of surface sites. This electrostatic attraction between the positively charged Pd@Ce-BDC and the anionic Cr(VI) species facilitates closer interaction and accelerates electron transfer, enhancing the reduction rate. Plots of relation between rate constant, % efficiency time were obtained for different catalytic dosage with constant conc. of Cr(VI) solution as shown in Figure 3f. The photocatalytic reduction of Cr(VI) generally occurs through multiple steps, starting with photoexcitation and the formation of reactive species. Among these, two active species superoxide radicals ($\boldsymbol{O_2^{-\bullet}}$) and photogenerated electron play an important role in the process. To gain insight into detailed role of active species, scavenger experiment was conducted using EDTA, isopropanol (IPA), silver nitrate ($AgNO_3$) and benzoquinone (BQ) to selectively quench **h⁺**, $\boldsymbol{OH^{\bullet}}$, electron and $\boldsymbol{O_2^{-\bullet}}$, respectively. As shown in Figure S5, adding EDTA had little effect on the reduction efficiency, suggesting that h^+ plays a minor role. However, the presence of $AgNO_3$ and BQ significantly decreased Cr(VI) reduction, indicating that electron and $\boldsymbol{O_2^{-\bullet}}$ are the main species driving the photocatalytic process[40, 41].

Catalytic reduction of 4-NP using Pd@Ce-BDC

Catalytic performance of Pd@Ce-BDC was evaluated by capturing UV-Vis spectra at regular time intervals, specifically tracking the decrease in absorbance at 400 nm, corresponding to the reduction of 4-NP. Figure 4a shows the time-dependent UV-Vis absorption spectra for the reduction of 4-NP using the catalyst. The catalytic performance of Ce-BDC in the reduction of 4-NP to 4-AP using $NaBH_4$ was assessed based on the key parameters such as pH, catalyst dosage, and overall reduction efficiency. In this reduction process, 4-NP exhibits a prominent absorption peak at 317 nm in the UV spectrum, which shifts to 400 nm after the addition of $NaBH_4$. This shift corresponds to the formation of 4-nitrophenolate ions. However, in the absence of a catalyst, no conversion of 4-NP was observed, even after 40 minutes, despite the reaction being thermodynamically feasible. This is because the reduction of 4-NP to 4-AP is kinetically hindered by a high energy barrier. The absorbance spectrum of the mixture of 4-NP and $NaBH_4$ remains unchanged even after two hours, indicating no reaction progression without a catalyst [42] as depicted in Figure 4b. Upon the addition of the catalyst, a blue shift in absorbance peak towards 298 nm, was observed, confirming the formation of 4-AP. Additionally, the isosbestic

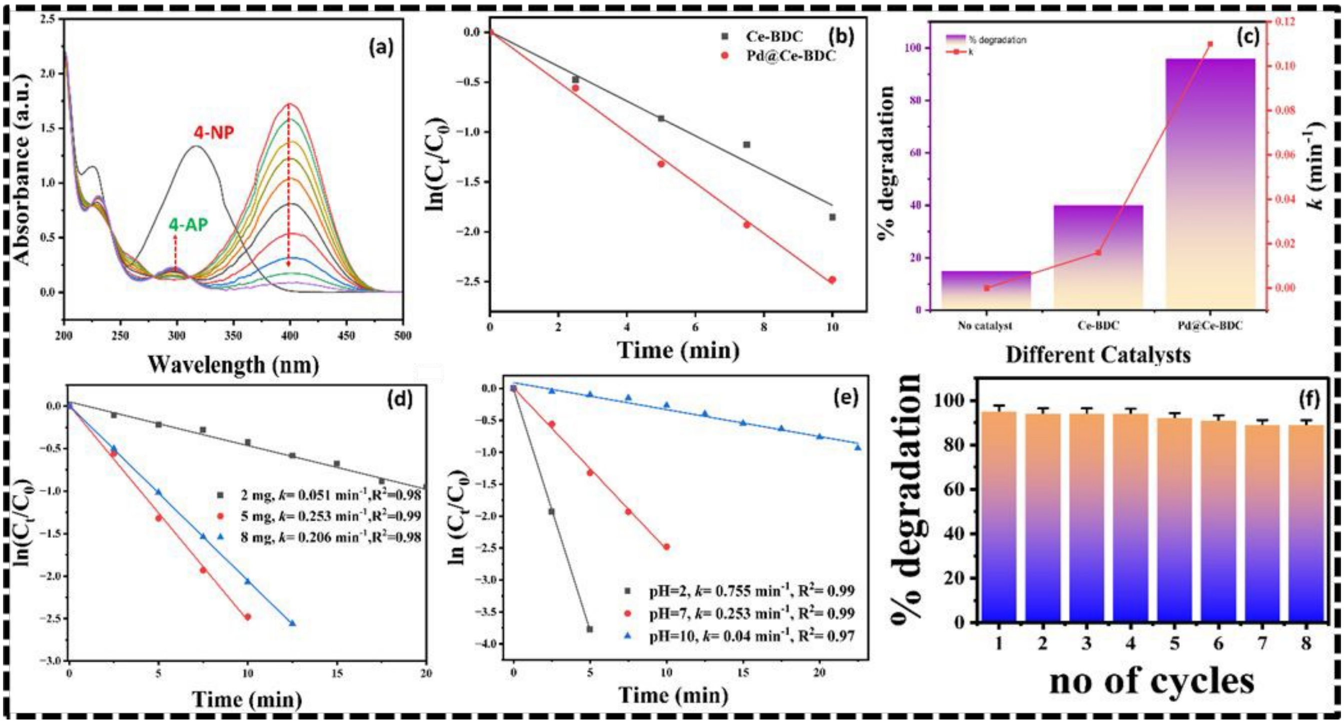

Figure 4: (a) Uv-Vis spectra **(b)**Pseudo-first-order kinetic models of 4-NP reduction using Ce-BDC and Pd@Ce-BDC**(c)**histogram of k value with % efficiency vs catalytic dosage for 4-NP reduction**(d)**ln(C_t/C_0) vs time at different pH for 4-NP reduction,**(e)** ln(C_t/C_0) vs time for different dosage, and**(f)** histogram showing reusability after 4-NP reduction.

point at 313 nm suggests that no side reactions occurred, and 4-AP was the sole product.[43] In the presence of excess $NaBH_4$, the reduction of 4-NP followed pseudo-first-order kinetics, described by the equation (eq. 3):

$$\boldsymbol{ln(C_0/C_t)} = -\boldsymbol{kt}\text{(eq.3)}$$

Where C⍰ is the concentration at time t, k is the pseudo-first-order rate constant, and C_0 is the initial concentration. The catalytic performance of Pd@Ce-BDC exhibits catalytic activity and follows pseudo first order kinetics[44]. It follows pseudo 1st order kinetics with rate constant 0.023 min^{-1} as shown in Figure 4d. The efficiency is attributed to the redox properties of cerium, particularly its facile Ce^{4+}/Ce^{3+} transition, which enhances electron transfer and accelerates reaction kinetics. Moreover, the increase in pH caused by excess $NaBH_4$ helps stabilize BH_4^- and suppress hydrolysis, ensuring that the catalytic effect is primarily governed by the metal centers in Pd@Ce-BDC. The conversion rate of 4-NP was calculated using the same equation applied for Cr(VI) reduction, as described in eq. 1.

The catalyst dosages were optimized by maintaining a constant concentration of 4-NP. By increasing the catalyst dosage from 2 mg to 8 mg significantly improved both the rate of reaction and reduction efficiency. The rate constant for 2 mg of Pd@Ce-BDC catalyst was found to be 0.051 min^{-1}, whereas at 5 mg, the rate of reaction and efficiency drastically increased to 0.253 min^{-1} and 95% respectively (Figure 4f). This increase in reaction rate with higher catalyst dosage is attributed to the availability of more active sites, allowing for greater interaction with the reactants, such as 4-NP. This enhancement is attributed to the increased availability of active sites, enabling greater interaction with 4-NP molecules.Further increase in catalyst dose to 8 mg the rate constant decreased to 0.206 min-1. This is because at higher catalyst loadings, particle aggregation reduces the effective active surface area.

The reduction rate of 4-NP is highly dependent on pH, as reflected in the present study, where the pseudo-first-order rate constant decreased when the pH increased from 2,7, and 11. By increasing the pH of solution from 2 to 11 the rate constant decreases from 0.755 min^{-1} to 0.04 min^{-1} as depicted in Figure 4d. Acidic conditions provide more protons (H^+), which are necessary for the reduction of the nitro group ($-NO_2$) to the corresponding amine ($-NH_2$). The reduction process typically involves the transfer of electrons and protons to the nitro group, so higher proton concentration speeds up the reaction. Plots of relation between rate constant, % efficiency time were obtained for different catalytic dosage with constant conc. of 4-NP solution as shown in Figure 4f.

Catalytic reduction mechanism

The plausible mechanism of photocatalytic reduction of Cr(VI) was explained below and illustrated in Figure 7. Upon exposure to visible light, electrons in the valence band (VB) are excited to conduction band (CB) generating excitons, also known as photogenerated free electron and holes in the CB and in VB respectively. In Ce-BDC, LMCT is strongly favoured especially for Ce^{4+} nodes, which have low-lying empty 4f orbitals in presence of light. This LMCT facilitates efficient separation of electrons and holes, reducing their rapid recombination and increasing carrier lifetime, thereby enhancing the photocatalytic activity.

The proposed mechanism of Cr(VI) reduction includes the following steps (eq. 4-11):

$$\boldsymbol{Pd@Ce-BDC+h\nu \rightarrow Pd@Ce-BDC\,(e^- + h^+)}\text{(eq. 4)}$$

$$\boldsymbol{O_2 + e^- \rightarrow O_2^{-\bullet}}\text{(eq. 5)}$$

$$\boldsymbol{O_2^{-\bullet} + Cr(IV) \rightarrow \mathrm{Cr(III)} + O_2}\text{ (eq. 6)}$$

$$\boldsymbol{h^+ + 2H_2O \rightarrow H^+ + 2OH^\bullet}\quad\text{(eq. 7)}$$

$$\boldsymbol{h^+ + 2H_2O \rightarrow 2H^+ + H_2O_2}\quad\text{(eq. 8)}$$

$$\boldsymbol{H_2O_2 + e^- \rightarrow OH^\bullet + OH^-}\quad\text{(eq. 9)}$$

$$\boldsymbol{O_2^{-\bullet}\,/\,OH^\bullet/\ +\ Cr(III) \rightarrow Cr(VI)}\text{ (eq. 10)}$$

$$\boldsymbol{Cr(VI) + 3e_{CB}^- \rightarrow \mathrm{Cr(III)}}\text{ (eq. 11)}$$

The photogenerated electron and superoxide radicals are mainly responsible for photocatalytic reduction of Cr(VI) which is evident from scavenger experiment. When BQ was added to the reaction system, the photocatalytic reduction efficiency was decreased from 95% to 61%, whereas with the addition of $AgNO_3$ supressed the photocatalytic activity up to 40% confirming their significant involvement in the reduction process. The production of photogenerated holes are responsible for production of hydroxyl radicals ($OH^\bullet$) from water and H_2O_2 indicating the conversion of Cr(III) to Cr(VI) via re-oxidation shown in Figure S5. The combined effects of charge carrier separation and the presence of reactive species drive the overall photocatalytic process, aligning with previously reported studies[45]. The plausible mechanism of reduction of 4-NP can be discussed by both electron transfer and redox property of Pd@Ce-BDC. Initially, BH_4^- ions and 4-NP molecules adsorb onto the Pd@Ce-BDC surface, facilitated by π–π interactions and electrostatic attractions between the negatively charged 4-NP and the Pd@Ce-BDC.Pd(0) nanoparticles adsorb BH_4^- and nitrophenol on their electron-rich surface. The small size and high dispersion of Pd(0) in supports like Ce-BDC maximize active sites and prevent agglomeration for sustained activity.This Cerium nano MOF appended Pd NPs stabilizes the hydride ion on its surface, hence smoothen the reduction.In contrast the redox property of Ce-BDC is further promoted by the intrinsic redox property of cerium centres (Ce^{3+}/ Ce^{4+}), which further transfer electrons in catalytic cycle. During catalysis, partial oxidation of Ce^{3+} to Ce^{4+} occurs upon electron donation, followed by regeneration of Ce^{3+} through interaction with $BH_4^-$for continuous electron flow.Overall, the superior catalytic activity arises from the synergistic interaction of Pd(0) nanoparticles and the redox-active Ce-BDC framework, where Pd/Ce interfacial charge transfer andreversible Ce^{3+}/Ce^{4+} redox cyclingcollectively promote efficient and sustained reduction of 4-nitrophenol[46]. The reusability of the Ce-BDC catalyst was also evaluated for both 4-NP and Cr(VI) reduction. Following each catalytic run, the material was recovered via centrifugation, rinsed thoroughly with methanol and water, and dried at 70 °C before reuse. Under optimized conditions, the efficiency for 4-NP reduction declined slightly from 95 % to 89 % after four successive cycles as shown in Figure 4f, whereas for Cr(VI)

View Article Online
DOI: 10.1039/D6LF00091E

reductionit dropped from 95 % to 90 % after three successive cycles as shown in Figure 3f. This gradual loss in activity can be ascribed to: (i) minimal leaching of Ce ions into the reaction medium, reducing the number of available active sites; (ii) slight mass loss during recovery and washing; and (iii) partial pore blockage by adsorbed intermediates or products. Despite this minor reduction in catalytic performance, PXRD patterns confirmed that the Ce-BDC retained its crystallinity and structural framework even after repeated use [41] as shown in Figure S8.

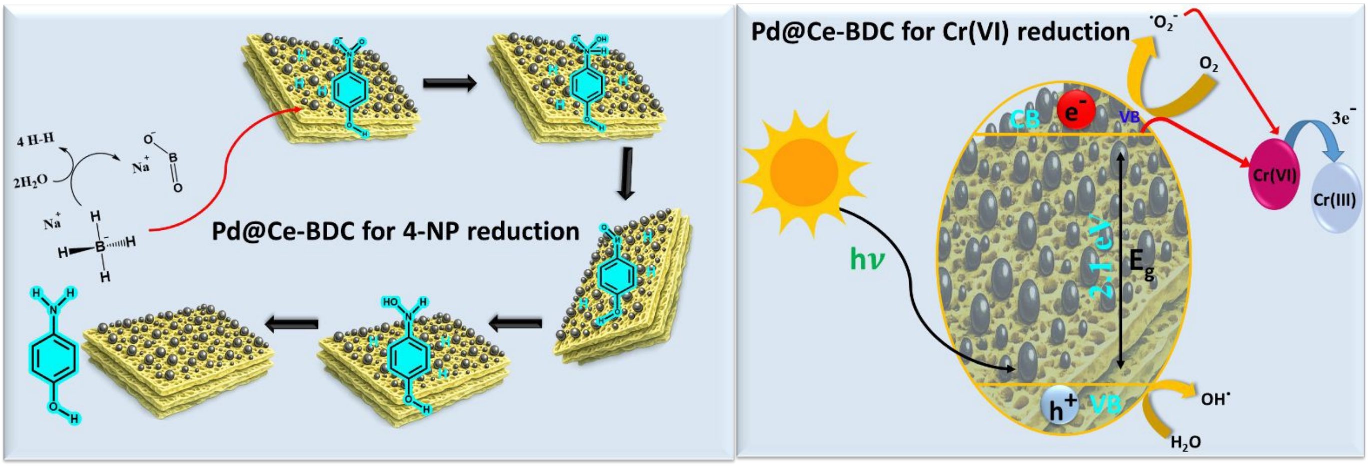

Figure 5: Plausible mechanistic pathway showing reduction of (a) Cr(VI) and (b) 4-NP

Conclusions

In summary, Ce-oxo SBU based MOF has been synthesized and deposition of Pd NPs creating interface, well characterized with standard method. The study reveals the formation of stable, redox as well as photoactive molecular system to achieve the ideal UiO-66 corresponds structural morphology. The well-defined porosity and molecular construction can be utilised in catalytic activity. Here, taking the advantage of chemical stability, photo harvesting property, and redox properties. it has been utilised for water purification through solar light, which is itself a green technology and a new way towards alternate source in view of energy crisis civilisation. In particular, at room temperature and neutral pH, 4-NP was completely reduced within just 10 minutes, while Cr(VI) reduction required around MIN minutes. Remarkably, Pd@Ce-BDC exhibited ~95% efficiency for 4-NP reduction and ~94% efficiency for Cr(VI) reduction under solar irradiation. The catalyst exhibited excellent reusability for eight consecutive cycles for reduction of 4-NP, and seven consecutive cycles for the reduction of Cr(IV), making it a sustainable photo catalyst for effective environmental remediation.

Conflicts of interest

There are no conflicts of interest to declare.

Acknowledgements

We acknowledge the Central Research Facility, KIIT for providing characterization facility and DRDO-DRDE project (LSRB/01/15001/LSRB-429/BTB/2024)for funding.

References

1. H. Kaur, S. Sinha, V. Krishnan and R. R. Koner, *Industrial & Engineering Chemistry Research*, 2020, **59**, 8538-8550.
2. A. O. Cardoso Juarez, E. Ivan Ocampo Lopez, M. K. Kesarla and N. K. R. Bogireddy, *ACS omega*, 2024, **9**, 33335-33350.
3. T. J. Martin, A. K. Goodhead, K. Acharya, I. M. Head, J. R. Snape and R. J. Davenport, *Environmental Science & Technology*, 2017, **51**, 7236-7244.
4. M. Lei, P. Wang, X. Ke, J. Xie, M. Yue, M. Zhao, K. Zhang, Y. Dong, Q. Xu and C. Zou, *Electron*, 2025, **3**, e43.
5. X. Zhao, Y. Chang, W.-J. Chen, Q. Wu, X. Pan, K. Chen and B. Weng, *ACS omega*, 2021, **7**, 17-31.
6. M. L. de Souza, D. P. Dos Santos and P. Corio, *RSC advances*, 2018, **8**, 28753-28762.
7. M. Yamada, M. Rajiv Gandhi and A. Shibayama, *Scientific Reports*, 2018, **8**, 16909.
8. X.-Z. Wei, H. Wang, J. Liu and L. Ma, *Inorganic Chemistry Communications*, 2023, **154**, 110956.
9. A. Lin, A. A. Ibrahim, P. Arab, H. M. El-Kaderi and M. S. El-Shall, *ACS Applied Materials & Interfaces*, 2017, **9**, 17961-17968.
10. B. Dutta, S. Datta and M. H. Mir, *Chemical Communications*, 2024, **60**, 9149-9162.
11. F. Zheng, S. Cao, Z. Yang, Y. Sun, Z. Shen, Y. Wang and H. Pang, *Energy & Fuels*, 2024, **38**, 11494-11520.
12. J. Panda, S. P. Biswal, H. S. Jena, A. Mitra, R. Samantray and R. Sahu, *Catalysts*, 2022, **12**, 494.
13. Y. Zhang, S. Liu, Z.-S. Zhao, Z. Wang, R. Zhang, L. Liu and Z.-B. Han, *Inorganic Chemistry Frontiers*, 2021, **8**, 590-619.
14. X.-P. Wu, L. Gagliardi and D. G. Truhlar, *Journal of the American Chemical Society*, 2018, **140**, 7904-7912.
15. M. D. Goudarzi, N. Khosroshahi and V. Safarifard, *RSC advances*, 2022, **12**, 32237-32248.
16. H. Zhao, X. Pang, Y. Huang, C. Ma, H. Bai and W. Fan, *Inorganic Chemistry*, 2022, **61**, 19806-19816.
17. M. Kohantorabi and M. R. Gholami, *Industrial & Engineering Chemistry Research*, 2017, **56**, 1159-1167.
18. M. Anandkumar, G. Vinothkumar and K. S. Babu, *New Journal of Chemistry*, 2017, **41**, 6720-6729.

19. H. M. Hassan, H. A. Alruwaili, M. S. Alhumaimess, A. H. Alanazi, M. El-Aassar, M. S. Alshammari, M. F. Hussein and I. H. Alsohaimi, *Environmental Research*, 2025, **264**, 120340.
20. X.-L. Xu, N.-N. Wang, Y.-H. Zou, X. Qin, P. Wang, X.-Y. Lu, X.-Y. Zhang, W.-Y. Sun and Y. Lu, *Nature communications*, 2024, **15**, 7273.
21. D. Grebenyuk, M. Shaulskaya, A. Shevchenko, M. Zobel, M. Tedeeva, A. Kustov, I. Sadykov and D. Tsymbarenko, *ACS omega*, 2023, **8**, 48394-48404.
22. G.-F. Liu, X.-X. Qiao, Y.-L. Cai, J.-Y. Xu, Y. Yan, B. Karadeniz, J. Lu and R. Cao, *ACS Applied Nano Materials*, 2020, **3**, 11426-11433.
23. C. Hu, Y.-C. Huang, A.-L. Chang and M. Nomura, *Journal of colloid and interface science*, 2019, **553**, 372-381.
24. K. Wang, D. Huang, X. Li, K. Feng, M. Shao, J. Yi, W. He and L. Qiao, *Electron*, 2023, **1**, e4.
25. S. Wunder, F. Polzer, Y. Lu, Y. Mei and M. Ballauff, *The Journal of Physical Chemistry C*, 2010, **114**, 8814-8820.
26. M. Lammert, C. Glißmann, H. Reinsch and N. Stock, *Crystal Growth & Design*, 2017, **17**, 1125-1131.
27. Z. Hu, Y. Wang and D. Zhao, *Chemical Society Reviews*, 2021, **50**, 4629-4683.
28. N. Nagarjun, P. Concepcion and A. Dhakshinamoorthy, *Applied Organometallic Chemistry*, 2020, **34**, e5578.
29. D. González, C. Pazo-Carballo, E. Camú, Y. Hidalgo-Rosa, X. Zarate, N. Escalona and E. Schott, *Dalton Transactions*, 2024, **53**, 10486-10498.
30. S. Sangeetha and G. Krishnamurthy, *Bulletin of Materials Science*, 2020, **43**, 269.
31. Q. Zhang, B. Yang, Y. Tian, X. Yang, R. Yu, J. Wang, T. Deng and Y. Zhang, *Green Processing and Synthesis*, 2022, **11**, 184-194.
32. J. He, C. Pei, Y. Yang, B. Lai, Y. Sun and L. Yang, *Journal of Cleaner Production*, 2021, **321**, 128778.
33. E. E. Ghadim, M. Walker and R. I. Walton, *Dalton Transactions*, 2023, **52**, 11143-11157.
34. M. Bagheri, A. Melillo, B. Ferrer, M. Y. Masoomi and H. Garcia, *ACS Applied Materials & Interfaces*, 2021, **14**, 978-989.
35. S. Karmakar, S. Barman, F. A. Rahimi, S. Biswas, S. Nath and T. K. Maji, *Energy & Environmental Science*, 2023, **16**, 2187-2198.
36. Y. Liu, G. Chen, J. Chen and H. Niu, *Catalysts*, 2022, **12**, 775.
37. X. Hu, J. Qian, J. Yang, X. Hu, Y. Zou and N. Yang, *Journal of Electroanalytical Chemistry*, 2023, **947**, 117756.
38. S. Rojas-Buzo, P. Concepción, J. L. Olloqui-Sariego, M. Moliner and A. Corma, *ACS Applied Materials & Interfaces*, 2021, **13**, 31021-31030.
39. Z. Kiani, R. Zhiani, S. Khosroyar, A. Motavalizadehkakhky and M. Hosseiny, *Inorganic Chemistry Communications*, 2021, **124**, 108382.
40. S. K. Sahoo and G. Hota, *ACS Applied Nano Materials*, 2019, **2**, 983-996.
41. J. Swain, A. Priyadarshini, S. Hajra, S. Panda, J. Panda, R. Samantaray, Y. Yamauchi, M. Han, H. J. Kim and R. Sahu, *Journal of Alloys and Compounds*, 2023, **965**, 171438.
42. Z. Valizadeh, S. M. Hosseini, R. Cheraghi and V. Safarifard, *Materials Research Bulletin*, 2025, **185**, 113304.
43. S. Gu, Y. Lu, J. Kaiser, M. Albrecht and M. Ballauff, *Physical Chemistry Chemical Physics*, 2015, **17**, 28137-28143.
44. M. Mansour, H. Kahri, M. Guergueb, H. Barhoumi, E. G. Puebla, B. Ayed and U. B. Demirci, *Reaction Chemistry & Engineering*, 2022, **7**, 908-916.
45. L. Shi, T. Wang, H. Zhang, K. Chang, X. Meng, H. Liu and J. Ye, *Advanced science*, 2015, **2**, 1500006.
46. X. Kong, H. Zhu, C. Chen, G. Huang and Q. Chen, *Chemical Physics Letters*, 2017, **684**, 148-152.

View Article Online
DOI: 10.1039/D6LF00091F

The datasets generated and/or analysed during the current study are available from the corresponding author upon reasonable request.